

THE PENNSYLVANIA STATE UNIVERSITY  
SCHREYER HONORS COLLEGE

DEPARTMENT OF MECHANICAL AND NUCLEAR ENGINEERING

**THE FLUID DYNAMICS OF HUMAN RESPIRATION AND OLFACTION**

STEPHANIE DOMBROWSKI  
Spring 2012

A thesis  
submitted in partial fulfillment  
of the requirements  
for the baccalaureate degree  
in Mechanical Engineering  
with honors in Mechanical Engineering

Reviewed and approved\* by the following:

Brent A. Craven  
Head, Computational Methods Development Department Applied  
Research Laboratory  
Thesis Supervisor

Zoubeida Ounaies  
Associate Professor in Mechanical Engineering  
Honors Advisor

\*Signatures are on file in the Schreyer Honors College

## **ABSTRACT**

The objective of this study is to examine the fluid dynamics of human respiration using a standardized three-dimensional model of the human nasal cavity. A brief background of the anatomy of the human nose is given along with references to other animals. Next, a surface model of the human nose is utilized to generate a high-fidelity computational mesh. The olfactory region of the airway is defined so airflow patterns in this area can be isolated. Assumptions and boundary conditions are specified for subsequent computational fluid dynamic (CFD) simulations. Using such techniques, simulations of inhalation and exhalation during respiration are compared. The results are analyzed and the effects of airflow patterns on olfaction are examined. Finally, the information gathered from this study regarding respiration and olfaction in humans is compared with other animals, thereby elucidating phenomena that may significantly contribute to mammalian olfactory acuity.

**TABLE OF CONTENTS**

Chapter 1 Introduction .....	1
The Human Nose .....	3
Anatomy .....	3
Physiology .....	4
Background.....	5
Objectives .....	6
Chapter 2 Methods .....	7
Surface Model.....	7
Assumptions .....	8
Boundary Conditions .....	13
Mesh Generation.....	14
Numerical Methods .....	16
Chapter 3 Results .....	18
Inspiration .....	18
Expiration .....	23
Chapter 4 Conclusions .....	28
Future Work.....	29

## ACKNOWLEDGEMENTS

I owe my deepest gratitude to my research supervisor, Dr. Brent Craven, whose encouragement, guidance and support from the initial to the final level enabled me to develop an understanding of fluid dynamics and CFD.

This thesis would not have been possible without the resources from the Garfield Thomas Water Tunnel and the Applied Research Laboratory.

Special thanks to Dr. Zoubeida Ounaies for advising me through the end of my undergraduate career.

Lastly, I would like to acknowledge the support of the Schreyer Honors College and the Pennsylvania State University.

## LIST OF FIGURES

Figure 1 - Canine versus human nasal cavity [2]. (a) A sagittal section of the canine nasal cavity. (b) A sagittal section of the human nasal cavity displaying the location of the olfactory region in yellow [3], [4], [1], [2]. .....	2
Figure 2 -The anatomy of the human nose [5].....	4
Figure 3–Surface model used in this study, comprised of the standardized nasal cavity geometry of Liu et al. [5] merged with a model of the external human head [8]. The respiratory airway is yellow, the olfactory airway is pink, the vestibule is blue, and nasopharynx is green.....	8
Figure 4 - Regional Distribution of the Womersley Number for Respiration .....	10
Figure 5 - Regional Distribution of the Womersley Number for Sniffing .....	11
Figure 6 - Regional Distribution of the Reynolds Number for Respiration .....	12
Figure 7 - Regional Distribution of the Reynolds Number for Sniffing.....	12
Figure 8 - (a) The pipe-like extension of the nasopharynx required for flow to become fully-developed. (b) Cross-section of nasopharynx. (c) The nasal cavity for visual reference. ....	13
Figure 9 - (a) Grid generated in the box surrounding the human head. (b) Refined region around the exterior of the nostril. ....	15
Figure 10 – A two-dimensional cross section of the fine mesh.....	16
Figure 11 - (a) Velocity contours for inspiration at five cross-sections through the human nasal cavity. (b) Location of the cross-sections within the nasal cavity...	19
Figure 12 - Streamlines of neutrally-buoyant particles through the human nasal cavity during inspiration .....	20
Figure 13 - Pressure contours on the surface of the right nasal cavity during inspiration. ....	21
Figure 14 - Wall shear stress contours on the surface of the right nasal cavity during inspiration.....	22
Figure 15 - a) Velocity contours for expiration at five cross-sections through the human nasal cavity. (b) Location of the cross-sections within the nasal cavity...	24

Figure 16 - Streamlines of neutrally-buoyant particles through the human nasal cavity during expiration.....	25
Figure 17 - Pressure contours on the surface of the right nasal cavity during expiration. ....	26
Figure 18 - Wall shear stress contours on the surface of the right nasal cavity during expiration. Scale same as Figure 14. ....	27

## **Chapter 1**

### **Introduction**

The fluid dynamics of human nasal airflow can be simulated to quantify the influence of airflow rate, inspiration versus expiration, and other parameters that affect respiration and olfaction (the sense of smell). In general, humans do not possess a keen sense of smell compared to other animals, such as the canine. Though canines have a larger surface area dedicated to olfaction [1] and more functional olfactory receptor genes [2], the significant disparity in canine versus human olfactory acuity has yet to be determined.

Compared to humans, the canine nasal cavity is significantly more complex, as illustrated in Figure 1. In particular, the canine possesses an “olfactory recess,” which is absent in humans, which likely affects nasal airflow patterns and olfaction [2]. However, a rigorous comparison of human versus canine olfaction has yet to be carried out, specifically, comparing the airflow patterns through the nose and how they vary with airflow rate, inspiration versus expiration, and other parameters.

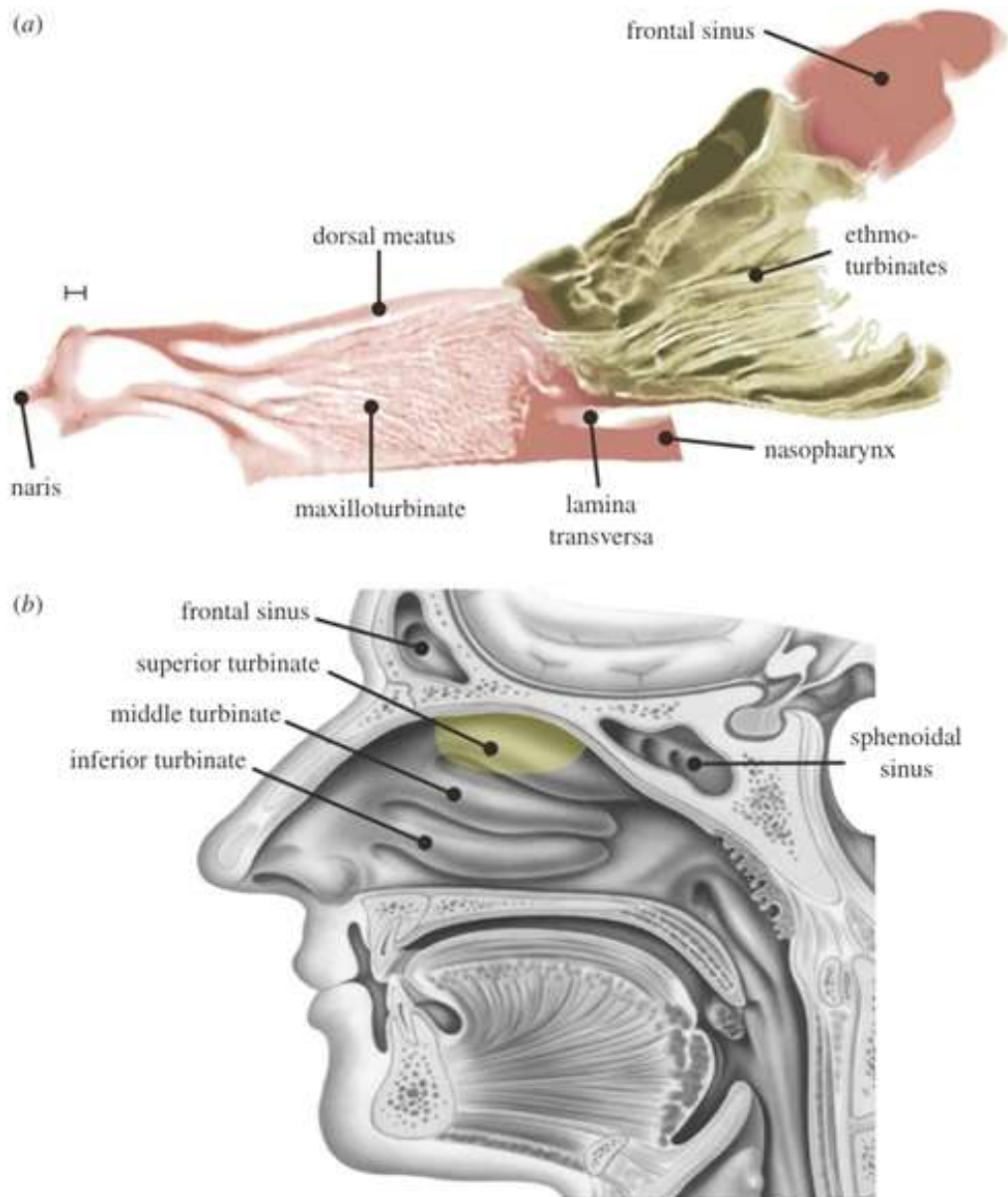


**Figure 1 - Canine versus human nasal cavity [2]. (a) A sagittal section of the canine nasal cavity. (b) A sagittal section of the human nasal cavity displaying the location of the olfactory region in yellow [3], [4], [1], [2].**

## **The Human Nose**

### **Anatomy**

The human nose is comprised of two bilaterally-symmetric cavities separated by the nasal septum. Because of this bilateral symmetry, this study will examine airflow through only one nasal cavity. Functionally, airflow enters the nasal cavity through the naris (or nostril) and subsequently flows through the vestibule, a large funnel-shaped region. The vestibule narrows and leads to the nasal valve, where the airway elongates and the main nasal passage begins. The “roof” of the nasal cavity is formed by bones and cartilage, and the “floor” is formed by the palate that separates the nasal and oral cavities [5].

The main nasal passage has three protrusions on the lateral (outside) wall called turbinates. The superior, middle, and inferior turbinates increase the exposed surface area to enhance heat and moisture exchange. The airways between the turbinates are called meatuses, and each meatus is named respectively for the turbinate above which it is located [6]. The anatomy of the human nasal cavity is shown in Figure 2. The olfactory region is located in the top of the main nasal airway, next to the superior turbinate, as shown in Figure 1(b).

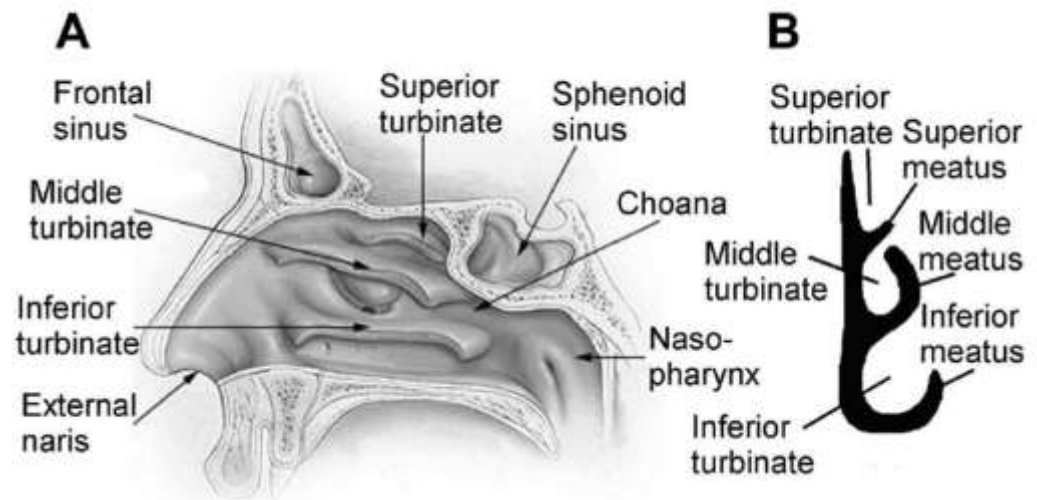


Figure 2 -The anatomy of the human nose [5].

### Physiology

The nose has three major functions: defense, air conditioning, and olfaction. Air is filtered in the nose before it flows into the lungs by trapping noxious vapor and particles in the respiratory mucosa that lines the majority of the nasal cavity. Simultaneously, the nasal cavity warms and humidifies air to a state where it can enter the lungs without causing damage to the alveolar lining (the lining in the lungs where gas exchange occurs). Finally, olfaction (the sense of smell) is facilitated when odorant molecules that are carried with the flow interact with olfactory receptors that are located in the olfactory region, shown in Figure 1(b).

## **Background**

The correlation between the structure and the function of the mammalian nasal cavity remains unclear, though recent studies [7] [2] [8] have begun to shed some light on comparative nasal function by examining nasal airflow in the human and the canine. Even so, a detailed comparison with the human is lacking because simulations and experiments to date have not considered the influence of airflow rate, inspiration versus expiration, and other parameters that affect nasal airflow patterns.

In general, odorant molecules must reach the olfactory region of the nasal cavity without being filtered by the respiratory airways. Thus, the fluid dynamic transport of molecules in the nasal cavity is the first fundamental step in olfaction. Previous studies have concluded that olfaction significantly depends on airflow patterns through the nasal cavity and the resultant transport of odorants [2]. Specifically, the existence of a highly-developed olfactory recess within the nasal cavity of macrosmats (keen-scented animals, like the canine) or the absence of one in microsmats (feeble scented animals, like the human) directly affects nasal airflow patterns and, thus, olfactory function and acuity [2]. By simulating human nasal airflow during inspiration and expiration, the resultant airflow patterns can be directly compared to other animals, which may be used to better understand why some animals have a keen sense of smell and others do not.

## **Objectives**

The objective of this study is to examine the fluid dynamics of human respiration and olfaction using a standardized three-dimensional model of the human nasal cavity. Using computational fluid dynamics (CFD), simulations of inspiration and expiration will be carried, resulting in three-dimensional nasal airflow patterns. These results will be examined and compared with other animals to further elucidate the possible role of such phenomena on the sense of smell.

## **Chapter 2**

### **Methods**

This section will describe the reconstructed anatomical model used in this study and the numerical methods, modeling assumptions, and boundary conditions. Also, the process of computational mesh generation will be explained.

#### **Surface Model**

This study utilized a three-dimensional surface model of the right human nasal cavity that was originally obtained from Liu et al. [5] and merged with a model of the human head by Shenk [8]. The final surface model can be seen in Figure 3. Only the right nasal cavity is modeled because of the bilateral symmetry and separation of the left and right nasal cavities. The anatomically-correct model of the nasal cavity was reconstructed from 30 CT scans of human nasal cavities in order to represent the general population. Since right and left nasal cavities may be different in an individual, both nasal cavities were analyzed to gather more data. By merging the standardized model of the nasal cavity with a model of the external head, the external flow can be simulated, which is required to accurately capture a physically-realistic inflow condition for inspiration [9].

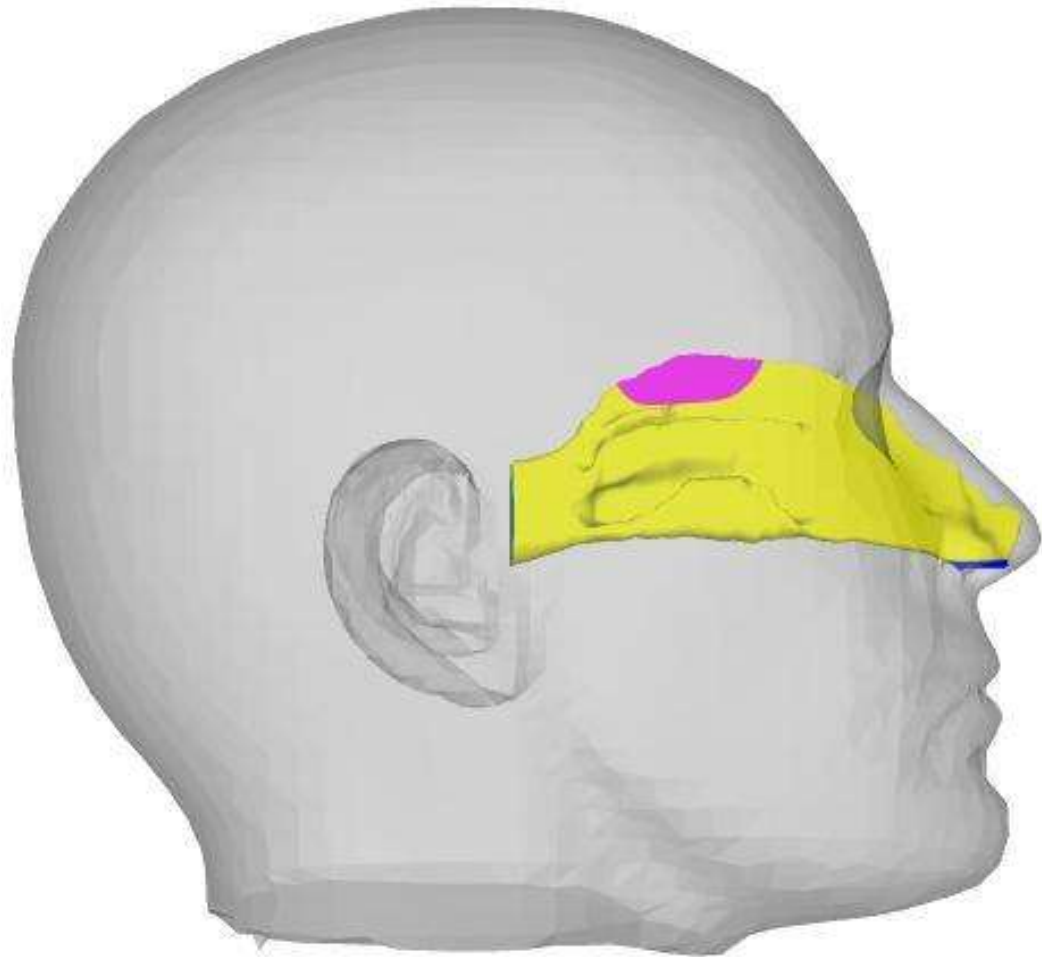


**Figure 3**–Surface model used in this study, comprised of the standardized nasal cavity geometry of Liu et al. [5] merged with a model of the external human head [8]. The respiratory airway is yellow, the olfactory airway is pink, the vestibule is blue, and nasopharynx is green.

### **Assumptions**

The internal turbinate structures of the nasal cavity are assumed to be rigid for the CFD calculation. Also, the nostril is static and undilated. The mucus layer that lines most of the nasal cavity is neglected in the CFD calculations for two reasons. First, the flow of mucus along the airway surface is slow [2]. Second, the thickness of this mucus layer

relative to the airways is extremely small [2]. Thus, the mucus layer has negligible effects on the fluid dynamics within the nasal cavity.

To determine the potential unsteadiness of the flow, the Womersley number,  $Wo_{D_h}$ , was calculated using Equation 1. When the Womersley number is less than 1, the flow is quasi-steady; when the Womersley number is greater than 1, the flow is considered fully unsteady. In the following equation,  $D_h$ , is the hydraulic diameter of the airway,  $f$  is the frequency of breathing or sniffing, and  $\nu$  is the kinematic viscosity of air. The frequency is 0.25 Hz for breathing [6] and 0.75 Hz for sniffing [3].

**Equation 1**

$$Wo_{D_h} = \frac{D_h}{2} \sqrt{\frac{2\pi f}{\nu}}$$

The nature of the flow, whether it is laminar or turbulent, depends on the presence of either quasi-steady or unsteady flow. For quasi-steady pipe flow, the velocity profile becomes unstable and transition to turbulence occurs when the Reynolds number is in the 2000-4000 range [2]. To evaluate whether the flow is laminar or turbulent, the Reynolds number,  $Re_{D_h}^{peak}$ , was calculated using Equation 2, where  $Q^{peak}$  is the peak inspiratory airflow rate,  $D_h$  is the hydraulic diameter of the airway,  $A_c$  is the cross sectional area, and  $\nu$  is the kinematic viscosity of air. The peak inspiratory airflow rate is 0.1 L/s for breathing [10] and 0.667 L/s for sniffing [3].

**Equation 2**

$$Re_{D_h}^{peak} = \frac{Q^{peak} D_h}{A_c \nu}$$

To evaluate Equation 1 and Equation 2, the three-dimensional model of the nasal cavity was sectioned into over 1000 transverse slices, and each slice was converted to a

binary image (black and white). A MATLAB program was used to morphologically erode the binary images, and these data were utilized by a separate MATLAB program that calculated hydraulic diameter, cross-sectional area, Womersley number, Reynolds number, and other properties at each transverse slice location. Using these data, axial distributions of Womersley and Reynolds numbers were calculated through the nasal cavity. Figure 4 and Figure 5 show the regional distribution of the Womersley number for breathing and sniffing, respectively.

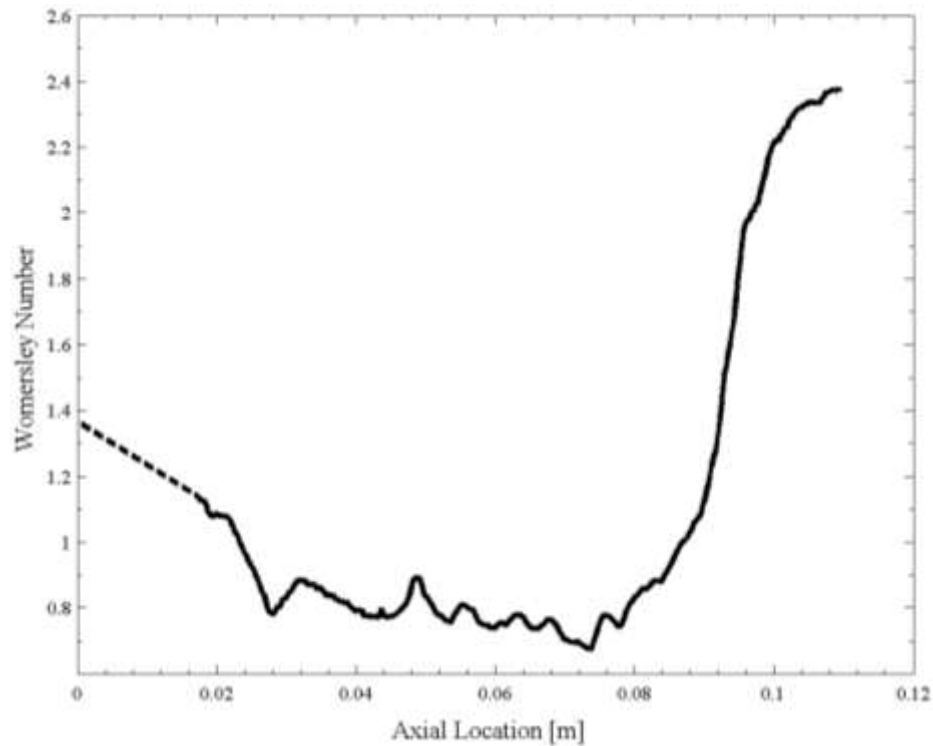


**Figure 4 - Regional Distribution of the Womersley Number for Respiration**

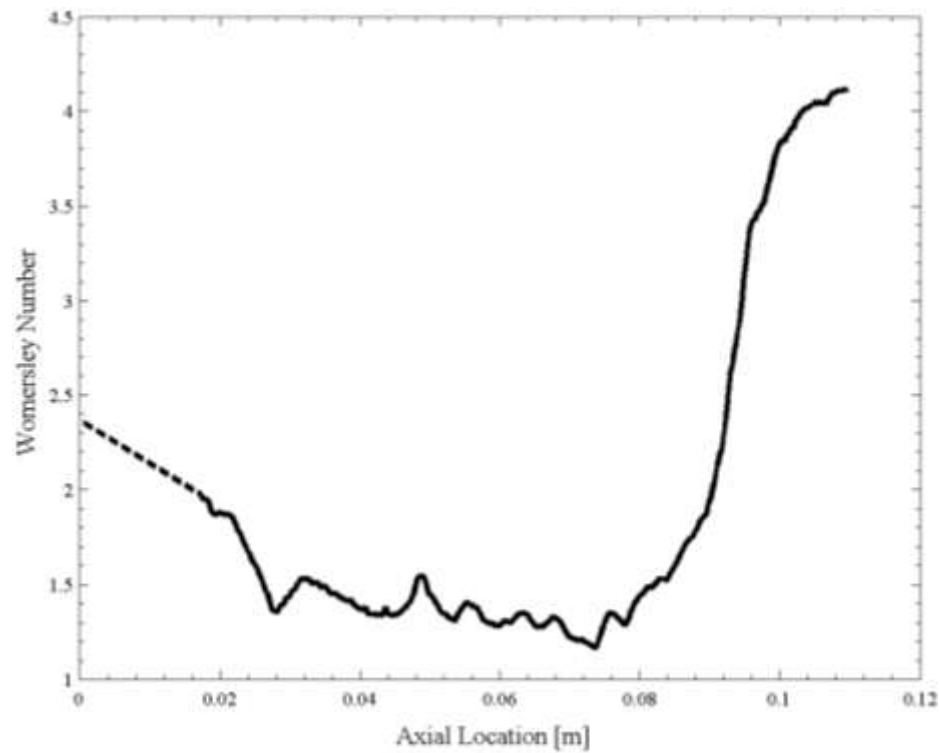


**Figure 5 - Regional Distribution of the Womersley Number for Sniffing**

Figure 6 shows the Reynolds number distribution in the nasal cavity during quasi-steady respiration, and Figure 7 illustrates the Reynolds number during peak inspiration of a sniff. The Reynolds number is plotted in the axial direction, from the naris to the nasopharynx. Given the low Reynolds numbers present during respiration, laminar airflow is assumed throughout the nasal cavity. The higher Reynolds numbers present in the sniffing case indicate that turbulent flow cannot be ignored. A turbulence model should be used to calculate airflow at peak inspiration.

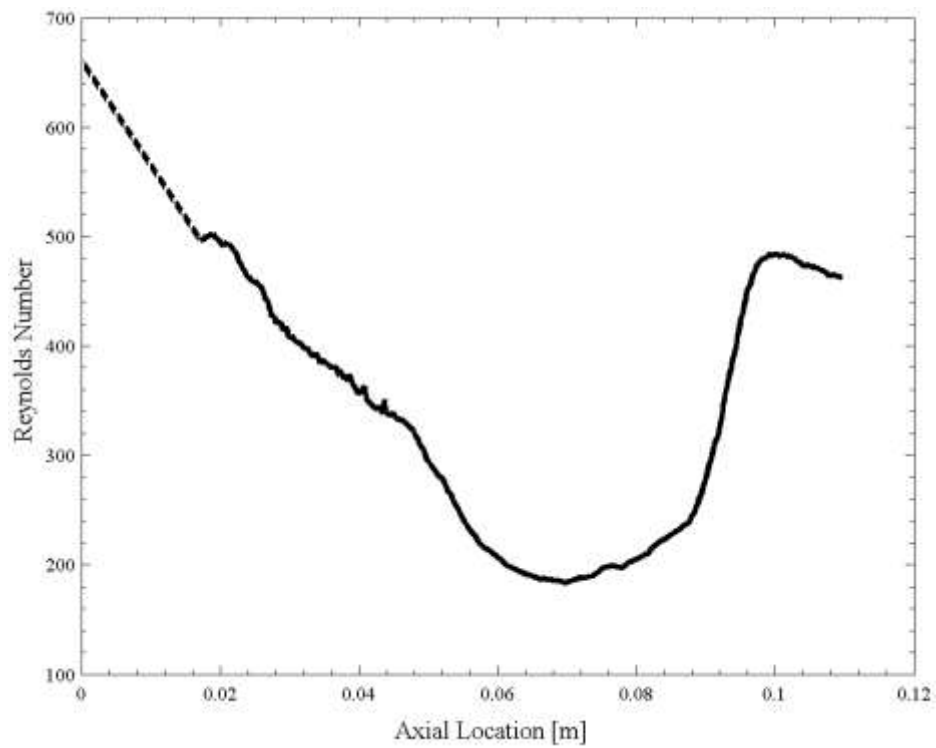


Figure 6 - Regional Distribution of the Reynolds Number for Respiration

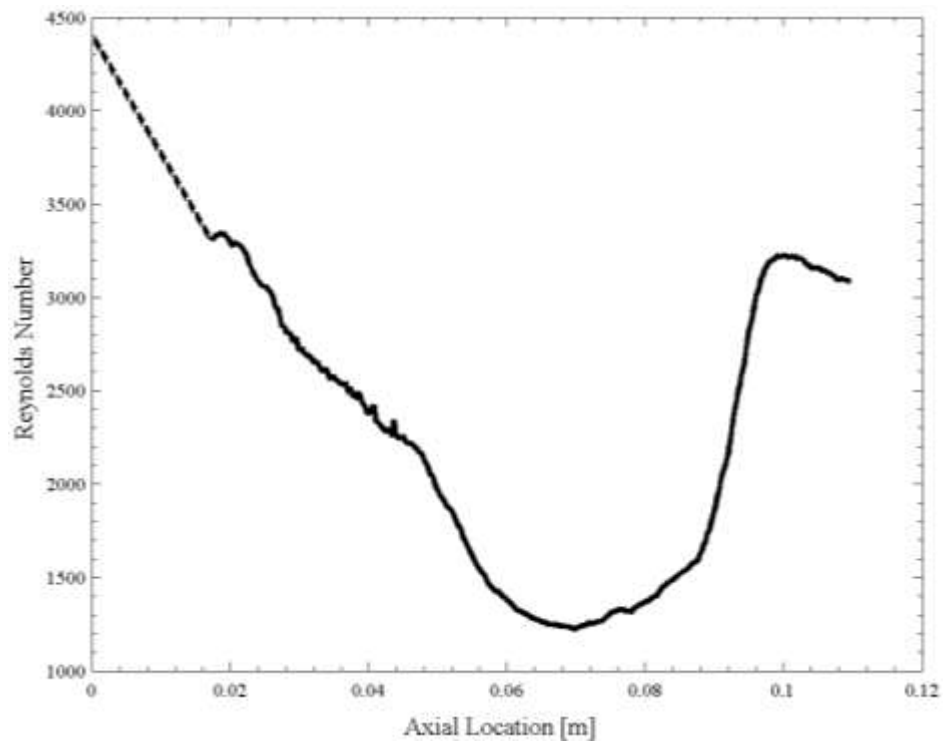


Figure 7 - Regional Distribution of the Reynolds Number for Sniffing

## Boundary Conditions

The computational domain consisted of the merged nasal airway model placed within a large computational “box.” The box permitted atmospheric pressure boundary conditions to be specified at a far field boundary, which was chosen to be large enough to avoid boundary effects on the airflow at the naris [2].

No-slip boundary conditions were applied on all solid surfaces since the mucus layer is negligible. Pressure boundary conditions were used at the nasopharynx and the far field boundary, with an overall pressure drop specified to drive the flow to match experimental airflow rates. For the respiration simulations, the computed volumetric airflow rate was 100 mL/s or 6 L/min [10]. To simulate reverse flow (an exhale instead of an inhale), the pressure difference between the nasopharynx and the far field boundary was switched, yielding approximately the same flow rate in the opposite direction.

In order to achieve fully-developed flow entering the nasopharynx during exhalation, special treatment of the inflow was required. First, the cross-section of the nasopharynx was extended to resemble a long pipe shaped like the nasopharynx. Figure 8(a) displays this extension of the nasopharynx, and Figure 8(b) shows the cross-section.



**Figure 8 - (a) The pipe-like extension of the nasopharynx required for flow to become fully-developed. (b) Cross-section of nasopharynx. (c) The nasal cavity for visual reference.**

The minimum length of the extension required for the flow to become fully-developed (i.e., the entrance length) was determined using Equation 3 and the calculated

Reynolds number,  $Re_{D_h}$ , and hydraulic diameter,  $D_h$ , found using the MATLAB program described above. From Figure 6, the Reynolds number at the location of the nasopharynx is 462, and the hydraulic diameter is 0.0149 m. Accordingly, Equation 3 yielded an entrance length of 0.345 m, which was used in specifying the length of the nasopharynx extension.

**Equation 3**

$$L_e = 0.05Re_{D_h}D_h$$

Next, a CFD simulation of flow through this "nasopharynx extension" geometry was used to calculate a "fully-developed" velocity profile that was subsequently used as the inflow boundary condition for the exhalation computation.

### **Mesh Generation**

A hybrid unstructured tetrahedral mesh was generated using ANSYS ICEMCFD. Separate grid resolutions and expansion ratios were assigned to the different parts of the geometry including the box, head, and nasal cavity sections such that the resolution could be precisely controlled in each of these regions. A coarse mesh was used in the far field region, and the grid density was refined in the head and external nose regions. The internal surfaces were given a finer grid density. Near-wall layers were added to the internal surfaces in order to better capture the boundary layer velocity gradients. Also, the region around the exterior of the nostril was refined to resolve the external inlet flow and can be seen in Figure 9(a). Figure 9(b) zooms in on the circular region in Figure 9(a) to show the refinement.

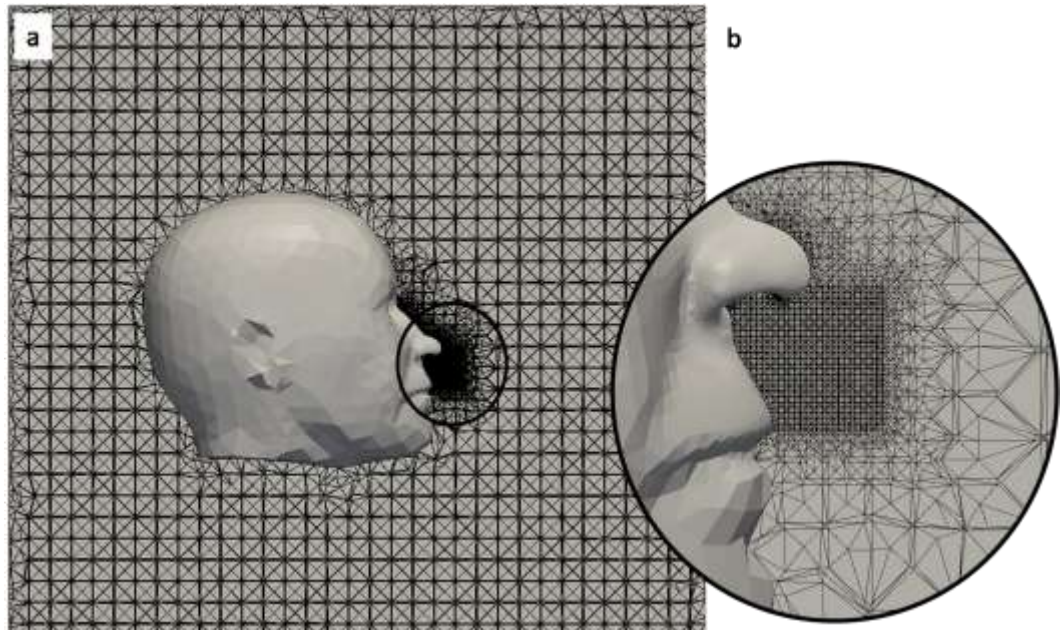


**Figure 9 - (a) Grid generated in the box surrounding the human head. (b) Refined region around the exterior of the nostril.**

Grid quality was enhanced as a post-processing step using a skewness-based smoothing algorithm [2]. The maximum mesh skewness was lowered as the highly-skewed cells were smoothed. Smoothing iterations were performed twice to optimize the grid quality.

Three different grids were generated: coarse, medium, and fine. They contained  $3.93 \times 10^6$  cells,  $9.509 \times 10^6$ , and  $17.799 \times 10^6$  computational cells, respectively. Figure 10 shows a two-dimensional cross section of the three-dimensional fine mesh. Figure 10(a) displays the entire cross-section and is similar in shape to Figure 2(b). Figure 10(b) zooms in on the superior meatus and the olfactory region of the nasal cavity contained by the rectangle in Figure 10(a) to highlight the grid refinement and the near-wall layers.

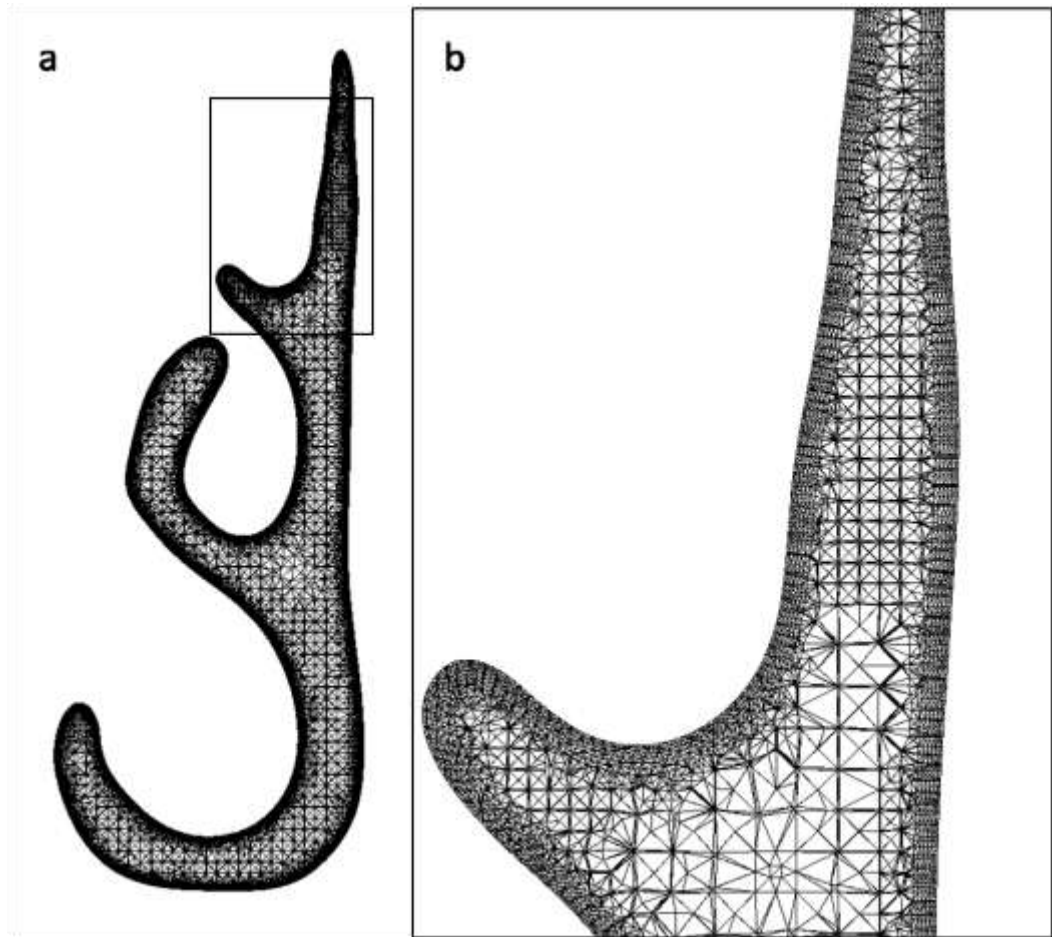


**Figure 10 – A two-dimensional cross section of the fine mesh.**

### **Numerical Methods**

The open-source computational continuum mechanics library OpenFOAM was utilized to simulate steady, laminar flow during respiration. Specifically, the second-order accurate semi-implicit method for pressure linked equations (SIMPLE) algorithm was used to solve the incompressible continuity and Navier-Stokes equations. Iterative convergence of the SIMPLE solver was guaranteed by forcing the solution residuals to be less than approximately  $10^{-3}$ . Additionally, various solution variables were monitored

throughout the simulation to ensure convergence of the computed result. Computations were performed on 80 processors of a high-performance parallel computer cluster at the Penn State Applied Research Laboratory.

## **Chapter 3**

### **Results**

#### **Inspiration**

Figure 11(a) shows coronal-plane velocity contours for the right human nasal cavity during inhalation. This figure begins with a cross-section of the naris region, and each subsequent cross-section moves toward the posterior of the nasal cavity in 0.0235 m increments. Figure 11(b) is included as a reference to show the location of each cross section within the nasal cavity. These results show that the highest velocities occur in the nasal valve and in the middle airways during inhalation. The olfactory region is located in the superior portion of the third and fourth cross-sections of Figure 11(a) (also refer to Figure 1(b)). As shown, this region encounters relatively low velocities during inhalation.

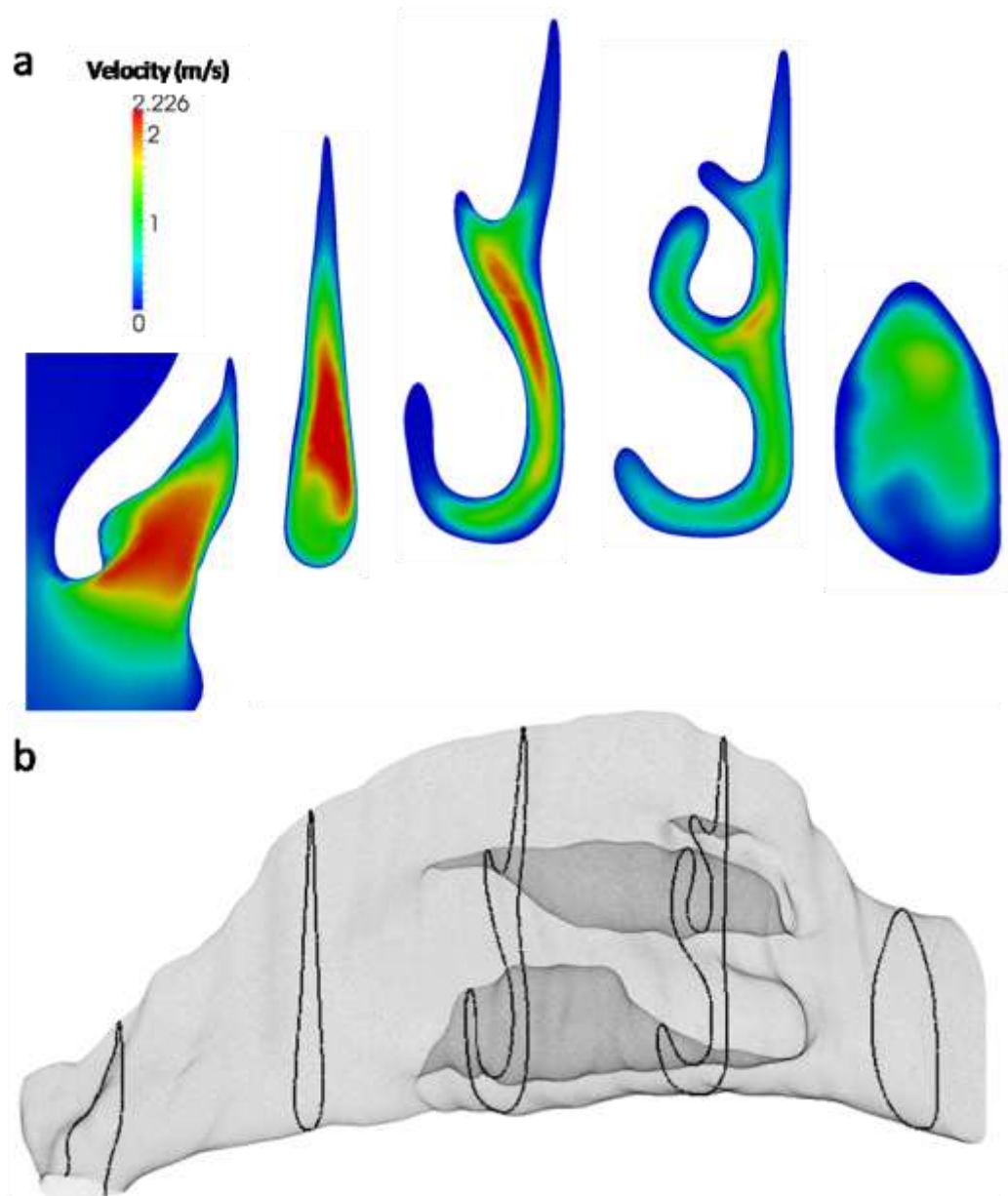


**Figure 11 - (a) Velocity contours for inspiration at five cross-sections through the human nasal cavity. (b) Location of the cross-sections within the nasal cavity.**

Figure 12 illustrates the airflow patterns in the right nasal cavity during inhalation. Specifically, the streamlines in this figure show the flow direction and velocity of neutrally-buoyant particles traveling through the nasal cavity. The streamlines that enter near the anterior portion of the naris travel through the superior portion of the

cavity, while the streamlines that enter near the posterior portion of the naris travel through the inferior section of the nasal cavity. The streamlines appear denser in the inferior and middle regions of the nose and less dense in the superior region. The streamlines in the superior portion pass through the olfactory region at relatively low velocities.

There are two regions of flow separation apparent in Figure 12. The first occurs in the superior part of the nasopharynx and is a result of airflow through the expansion of the nasopharynx. The other region of separated flow occurs in the vestibule, which is also caused by the rapid expansion of the nasal cavity downstream of the naris.

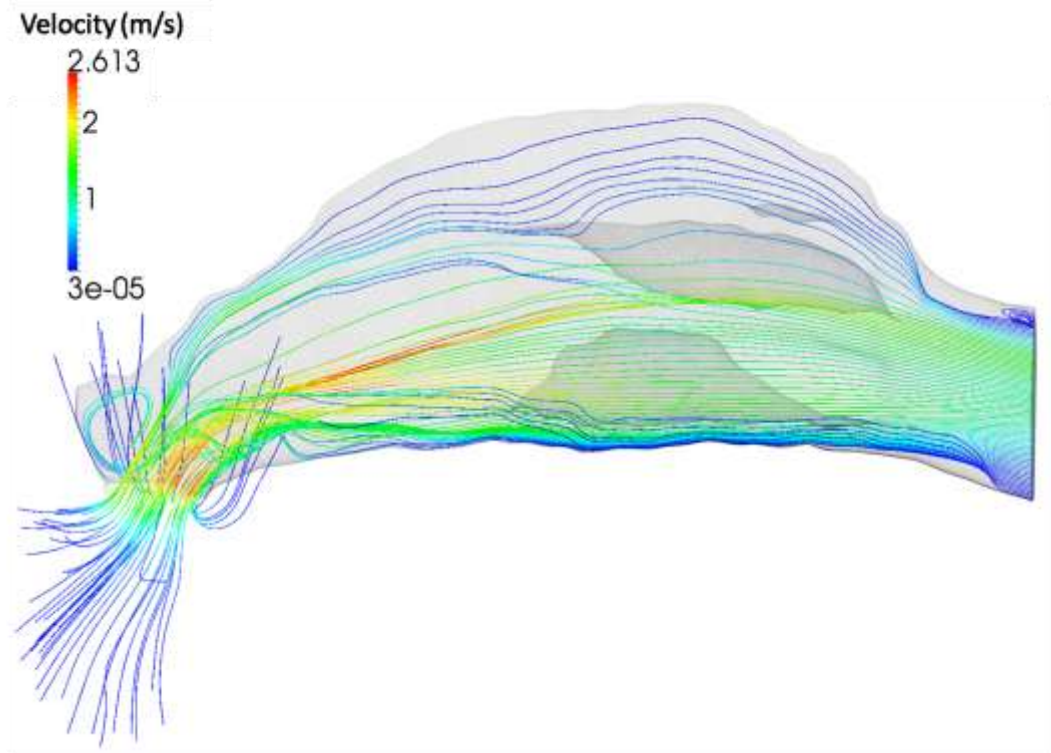


**Figure 12 - Streamlines of neutrally-buoyant particles through the human nasal cavity during inspiration**

Figure 13 shows the pressure distribution along the walls of the nasal cavity during inhalation. The maximum pressure occurs near the vestibule and in the superior

region of the nasal valve. There is high pressure in these regions because of the airflow colliding (or impinging) on the surface of the nasal cavity as it accelerates through the nasal valve. The minimum pressure occurs in the nasopharynx.

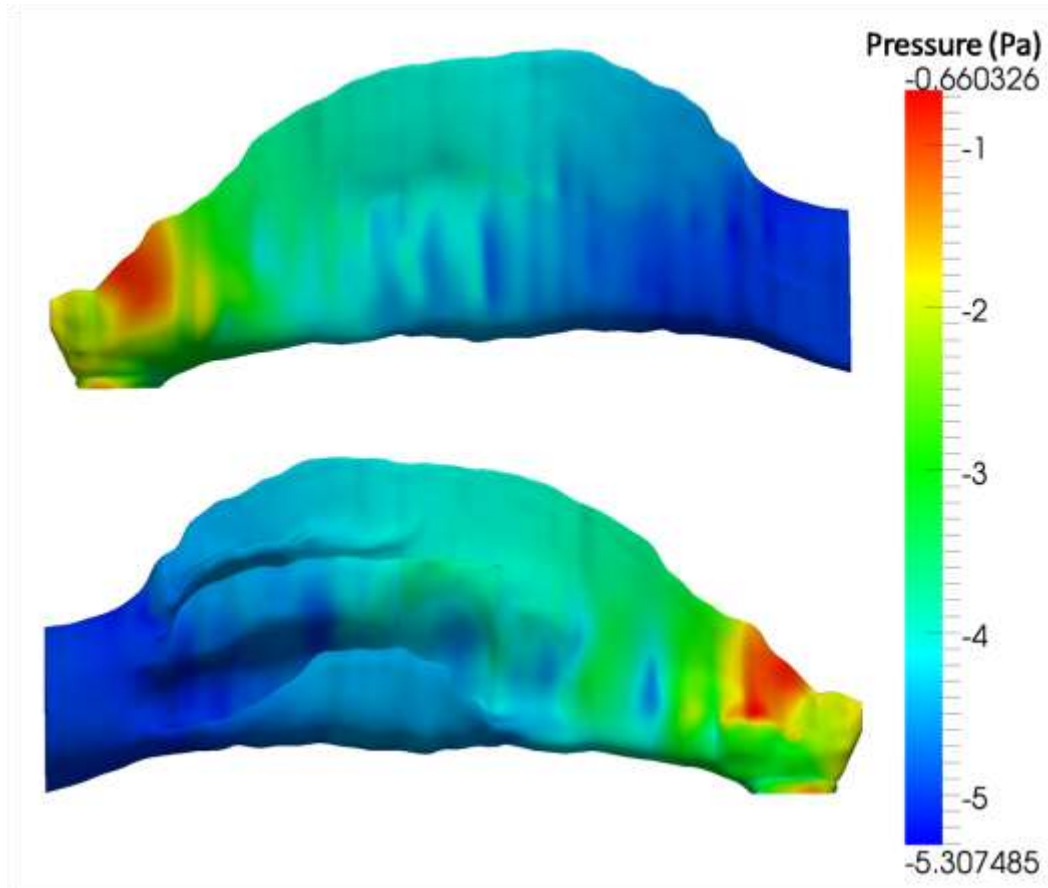


**Figure 13 - Pressure contours on the surface of the right nasal cavity during inspiration.**

Figure 14 displays contours of wall shear stress along the nasal cavity during inspiration. The areas of higher wall shear stress appear to occur in regions that correspond to airway constrictions. Physically, this occurs because the flow accelerates through these constrictions, which causes higher velocity gradients at the wall (i.e., shear stress).

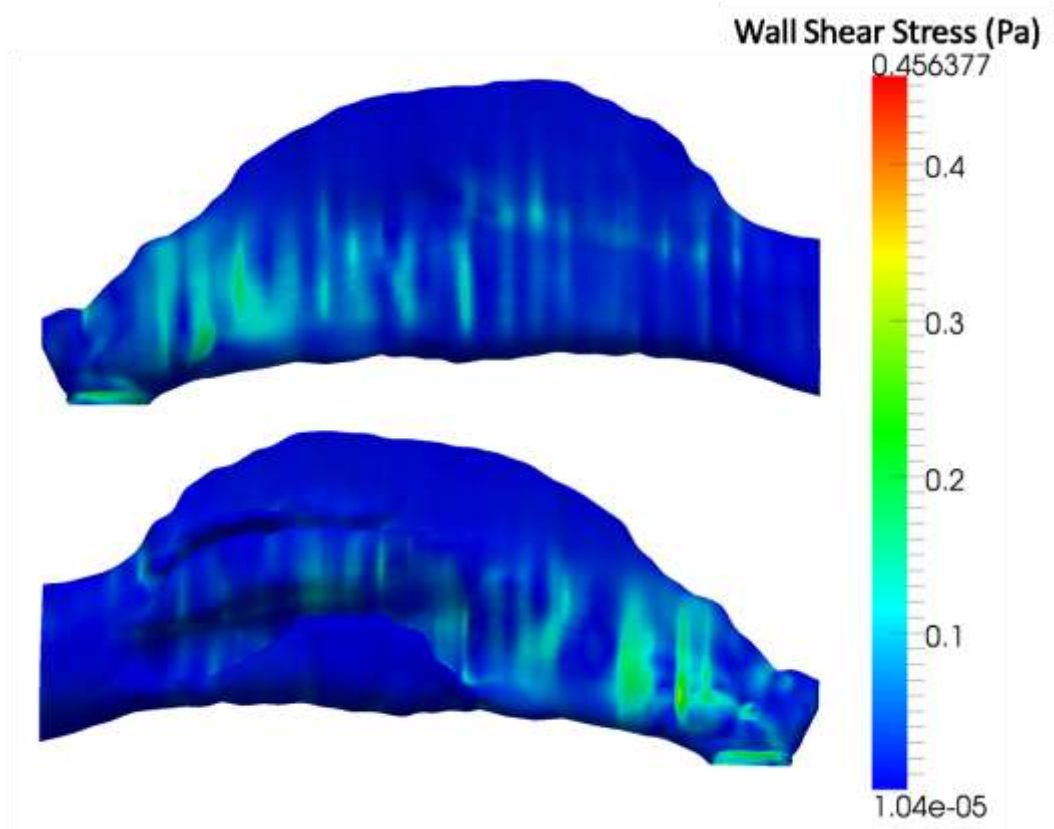
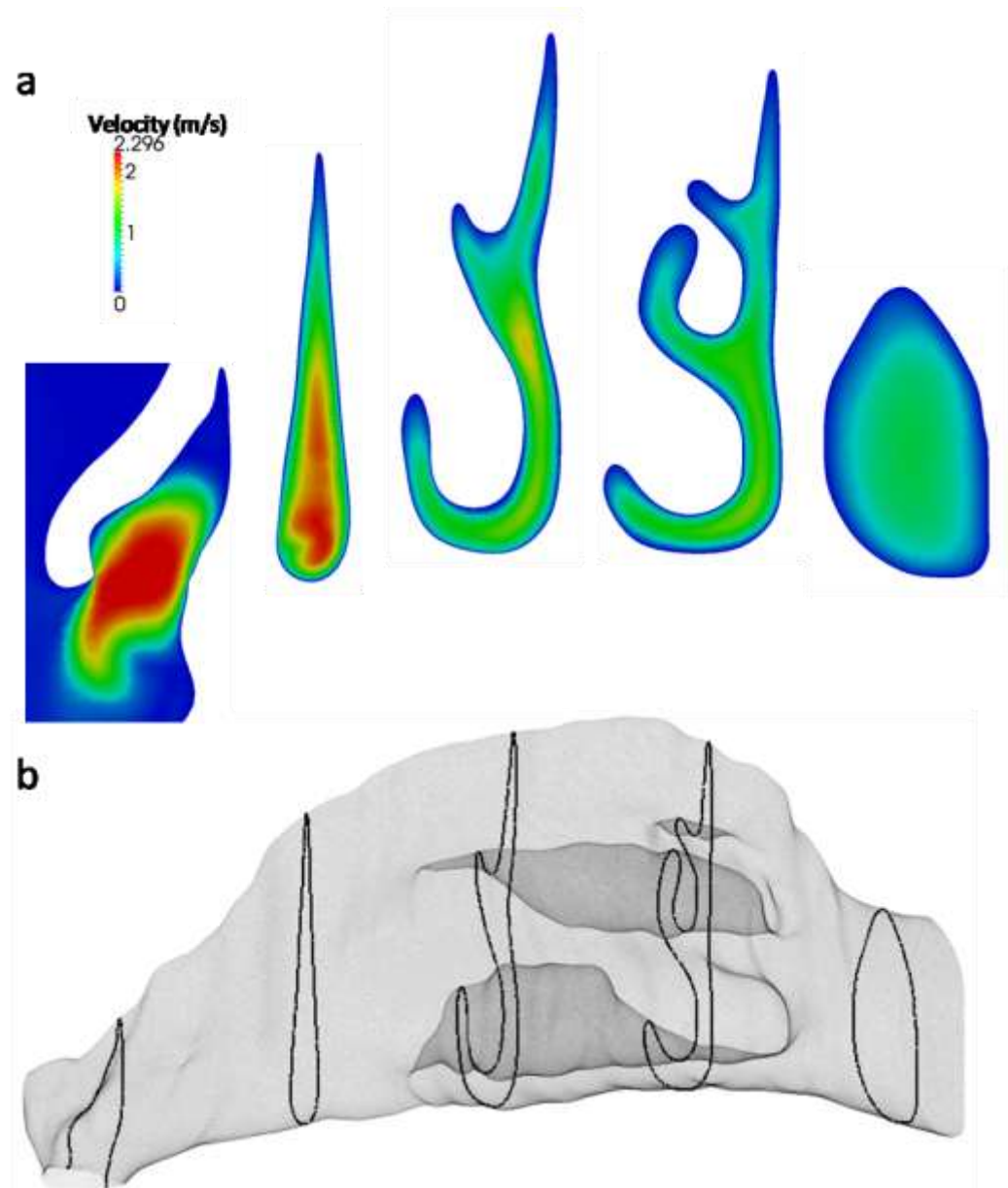


Figure 14 - Wall shear stress contours on the surface of the right nasal cavity during inspiration.

## **Expiration**

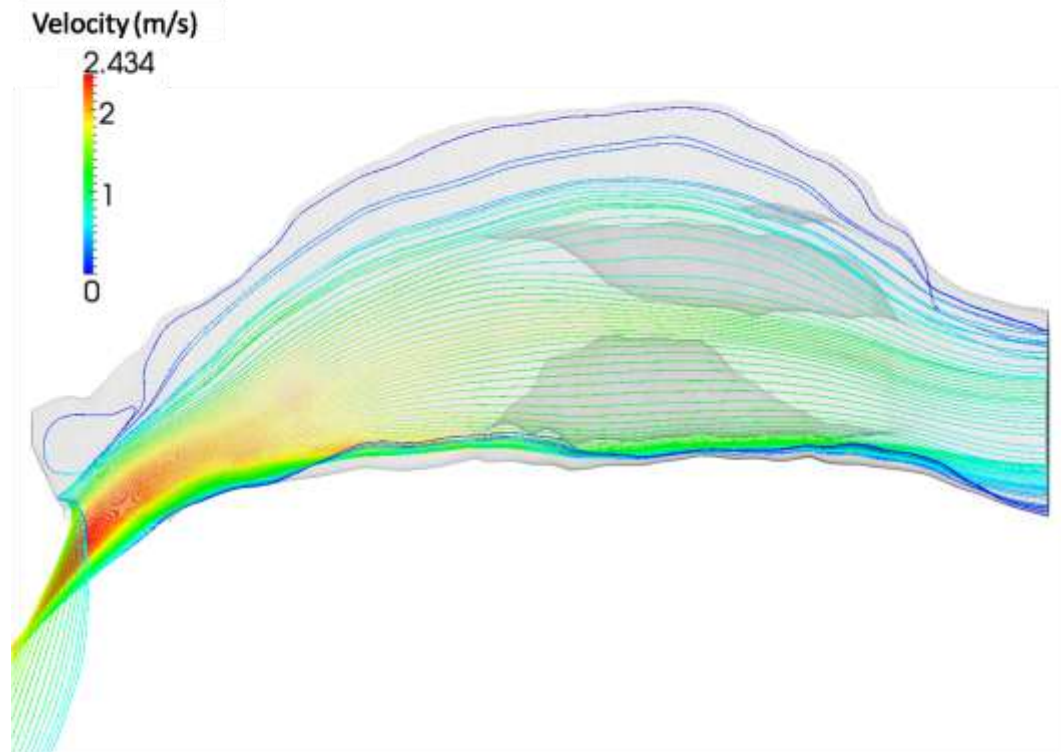
Figure 15(a) shows coronal-plane velocity contours for the right human nasal cavity during expiration. Figure 15 shows that the highest velocities occur in the nasal valve region during exhalation. The olfactory region, located in the superior portion of the third and fourth cross-section of Figure 15(a) encounters relatively low velocities during exhalation. Even so, airflow during expiration appears to be more uniformly distributed within the nasal cavity compared to airflow during inspiration (see Figure 11).



**Figure 15 - a) Velocity contours for expiration at five cross-sections through the human nasal cavity. (b) Location of the cross-sections within the nasal cavity.**

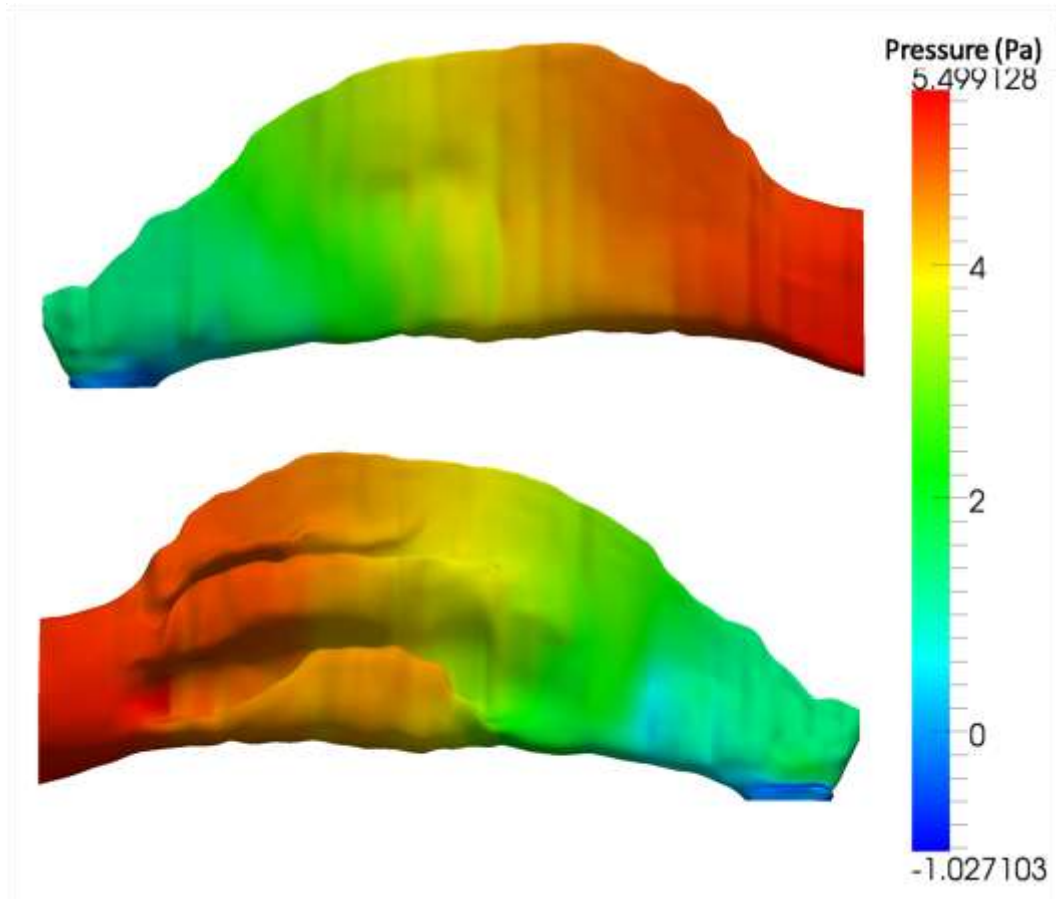
Figure 16 shows airflow patterns in the right nasal cavity during exhalation. The streamlines that enter near the superior portion of the nasopharynx travel through the superior portion of the nasal cavity and exit through the anterior portion of the naris; and the streamlines that enter near the inferior portion of the nasopharynx travel through the

inferior and middle portion of the nasal cavity and exit through the posterior portion of the naris. The streamlines appear most dense in the middle region of the nasal cavity and least dense in the superior region. The streamlines in the superior portion pass through the olfactory region at relatively low velocities.



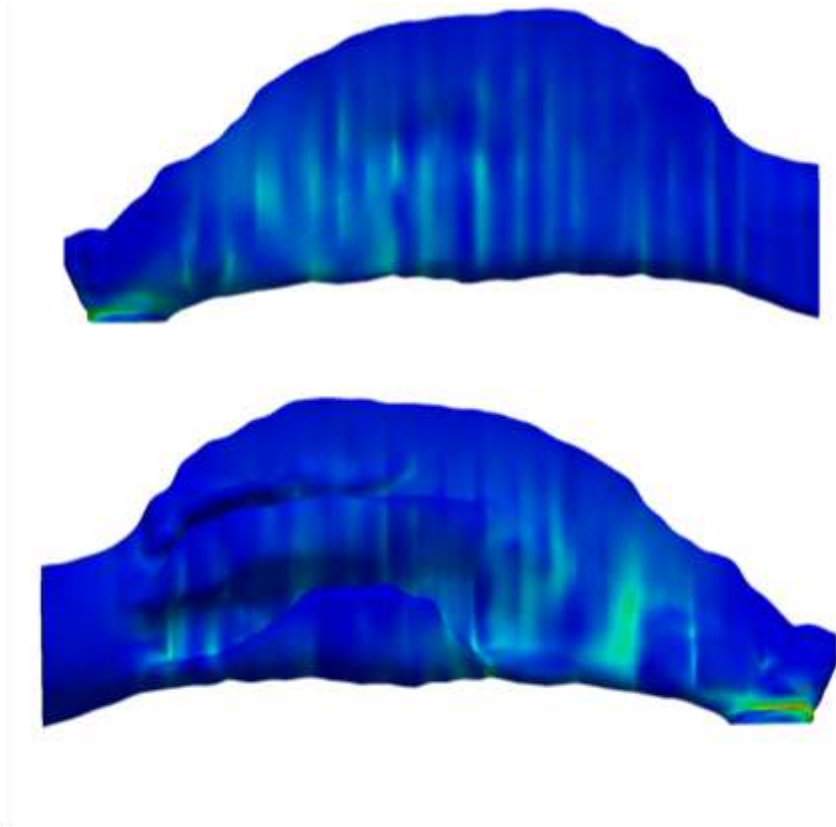
**Figure 16 - Streamlines of neutrally-buoyant particles through the human nasal cavity during expiration**

Figure 17 illustrates the pressure distribution along the walls of the nasal cavity during expiration. The maximum pressure occurs in the nasopharynx and the pressure gradient steadily decreases to the minimum pressure at the naris.



**Figure 17 - Pressure contours on the surface of the right nasal cavity during expiration.**

Figure 18 displays contours of wall shear stress on the nasal cavity during expiration. As with inspiration, the constriction of the nasal cavity near the naris leads to high shear stress values at this location.



**Figure 18 - Wall shear stress contours on the surface of the right nasal cavity during expiration. Scale same as Figure 14.**

## Chapter 4

### Conclusions

Airflow patterns through the human nose are determined by the complex structure of the nasal cavity. This study used the open-source computational continuum mechanics library OpenFOAM to simulate quasi-steady, laminar flow during respiration using a three-dimensional surface model of the right human nasal cavity, originally obtained from Liu et al. [5] and merged with a model of the human head by Shenk [8]. Both inspiration and expiration simulations were modeled for respiratory airflow rates, and the velocity profiles, streamlines, and pressure and wall shear stress contours were compared.

Both inspiration and expiration simulations showed that the airflow through the olfactory region travels at low velocity compared to the airflow through the middle region of the nasal cavity. The low velocity airflow through the olfactory region may facilitate the deposition of odorant molecules on the olfactory epithelium, while protecting the sensitive olfactory receptor neurons from noxious chemicals.

The olfactory recess in macrosmatic animals (such as the canine) allows olfactory stimulation to continue throughout expiration since airflow does not pass through this region during expiration [2]. However, the olfactory region in the microsmatic human nasal cavity is located in the main airway so olfactory stimulation cannot continue throughout expiration. From the present results, the olfactory region is cleared of inspired odorants and new odorants may pass through this region during expiration via the retro-nasal route. Thus, the findings of this study support the hypotheses of Craven et al. [2], whereby the function and acuity of mammalian olfaction depends on the anatomy of the

nasal cavity and the airflow patterns created by the presence or absence of an olfactory recess.

### **Future Work**

Future studies should examine the effects of higher flow rates associated with sniffing on airflow patterns in the nasal cavity and in the olfactory region. Additionally, future studies should consider the influence of unsteadiness of airflow in the nose.

## BIBLIOGRAPHY

- [1] B. Craven, T. Neuberger, E. Paterson, A. Webb, E. Josephson and E. & S. G. Morrison, "Reconstruction and morphometric analysis of the nasal airway of the dog (*Canis familiaris*) and implications regarding olfactory airflow," *The Anatomical Record: Advances in Integrative Anatomy and Evolutionary Biology*, vol. 290, pp. 1325-1340, 2007.
- [2] B. Craven and E. & S. G. Paterson, "The fluid dynamics of canine olfaction: unique nasal airflow patterns as an explanation of macrosmia," *Journal of The Royal Society Interface*, vol. 7, p. 933, 2010.
- [3] D. Hornung, "Nasal anatomy and the sense of smell," *ADVANCES IN OTORHINOLARYNGOLOGY*, vol. 63, p. 1, 2006.
- [4] J. Lang, *Clinical anatomy of the nose, nasal cavity and paranasal sinuses*, 1989.
- [5] Y. Liu, M. Johnson, E. Matida and S. & M. J. Kherani, "Creation of a standardized geometry of the human nasal cavity," *Journal of Applied Physiology*, vol. 106, pp. 784-795, 2009.
- [6] K. Keyhani and P. & M. M. Scherer, "Numerical simulation of airflow in the human nasal cavity," *Journal of biomechanical engineering*, vol. 117, p. 429, 1995.
- [7] B. Craven, E. Paterson and G. & L. M. Settles, "Development and verification of a high-fidelity computational fluid dynamics model of canine nasal airflow," *Journal of Biomechanical Engineering*, vol. 131, p. 091002, 2009.
- [8] E. M. Shenk, "A computational study of airflow in a standardized human nasal cavity : implications regarding olfaction," 2010.
- [9] D. Doorly, D. Taylor, A. Gambaruto and R. & T. N. Schroter, "Nasal architecture: form and flow," *Philosophical Transactions of the Royal Society A: Mathematical, Physical and Engineering Sciences*, vol. 366, pp. 3225-3246, 2008.
- [10] D. a. D. D. a. S. R. Taylor, "Inflow boundary profile prescription for numerical simulation of nasal airflow," *Journal of The Royal Society Interface*, vol. 7, pp. 515-527, 2010.

- [11] S. & H. J. Kim, "An investigation on airflow in pathological nasal airway by PIV," *Journal of Visualization*, vol. 7, pp. 341-348.
- [12] D. Doorly and D. & S. R. Taylor, "Mechanics of airflow in the human nasal airways," *Respiratory physiology & neurobiology*, vol. 163, pp. 100-110, 2008.

**VITA**  
Stephanie Dombrowski

**Permanent Address:**

106 Pine Acre Lane  
Moon Township, PA 15108

**Education:**

**Major:** Mechanical Engineering

**Minor:** Engineering Mechanics

**Honors:** Mechanical Engineering

**Thesis Title:** The Fluid Dynamics of Human Respiration and Olfaction

**Thesis Advisor:** Zoubeida Ounaies

**Research Advisor:** Brent A. Craven

**Work Experience:**

May 2010 – May 2012

Honors Undergraduate Research Assistant

Researched Computational Fluid Dynamics Modeling of Human Respiration

Applied Research Lab, Penn State University, University Park, PA 16802

Dr. Brent A. Craven